Experimental and numerical studies on flood inundation processes over a typical urban street

Boliang Dong[1], Junqiang Xia*[1], Meirong Zhou[1], Shanshan Deng[1],
Reza Ahmadian[2], Roger A. Falconer[2]

1 State Key Laboratory of Water Resources and Hydropower Engineering Science, Wuhan University, Wuhan 430072, China; Email: xiajq@whu.edu.cn
2 School of Engineering, Cardiff University, Cardiff, CF24 3AA, UK

Abstract:

Accurate prediction of flood inundation processes in urban areas is challenging due to the complexity of street layouts and the variety of infrastructures. In this study, based on a laboratory model of urban flooding with a sewer system underneath, a series of laboratory experiments were conducted to investigate the influences of different street layouts and infrastructures on flood inundation processes. Key hydrographs of water depth and flow velocity were recorded at several measurement points to provide comprehensive information about the hydrodynamic characteristics of urban flooding. Furthermore, a 2D shallow water equations model based on the finite volume method was also utilized to replicate the experimental scenarios considered. An analysis of the mesh resolution and discharge capacity formulae for street inlets were also performed through a series of numerical tests. The following conclusions are drawn from this study: (i) the sewer system has a strong influence on the flood inundation processes in terms of reducing both the surface water depth and flood wave velocity, as compared with street layouts and other infrastructures; (ii) the results from the numerical simulations agree well with the experimental findings, with the NSE values being greater than 0.9 and the RMSE values less than 1.5×10^{-3}; (iii) the marginal effect of increasing the mesh resolution is significant, which means a further increment in the mesh resolution may benefit slightly the numerical model predictions, but at the expense of an increasing computational cost; and

(iv) of all the inlet discharge capacity formulae used in this study, the weir and orifice formulae considering the influence of rain boxes were the most appropriate for representing the geometric features of street inlets and showed the best performance in calculating the flow exchange between surface runoff and underground sewer system.

Keywords: Urban flood, flood inundation, laboratory experiments, numerical modelling, street inlets, inlet discharge capacity formulae

1 Introduction

Flooding is the most common natural disaster world-wide and has become a major threat to people and property in urban areas. The frequency of occurrence and intensity of urban flood events are rising gradually, due to global climate change, increasing population and rapid urbanization. From 1995 to 2015, nearly half of the natural disasters globally were associated with floods, leading to 56% of the total number of victims suffering from any type of natural disaster (UNDRR, 2019). For example, 14 people died and 2,3600 buildings were destroyed in a recent extreme flood event in Wuhan City, China, with 757,000 people being affected as a result of the 2016 flood event (Cheng et al., 2019). Therefore, it is important to understand the causes and consequences of urban flooding and to develop accurate modelling methods for predicting the flood inundation processes in urban regions.

Field data for urban floods, such as aerial photography and watermarks, are generally insufficient for accurate model validation and such data are limited in representing the complexity of flood inundation extent, particularly for extreme flood events (Puech and Raclot, 2002; Chen et al., 2017). In recent years, a series of experimental studies have been undertaken to better understand flood inundation processes, as well as the interaction between floodwaters and infrastructures in urban areas (Mignot et al., 2019). In addition, these experimental studies have provided a reliable dataset for the validation of numerical models. Water depth and flow velocity are the key parameters to describe the characteristics and disaster-causing mechanisms of urban flooding. In most laboratory experimental studies, the results are acquired by using several water gauges and/or well-established sensing techniques, such as PIV (Particle Image Velocimetry) and RGB-D (red-green-blue-depth) (Soares-Frazão and Zech, 2007; Aureli et al., 2015; Martínez-Aranda et al., 2018). In comparison to using a limited number of gauges, sensing techniques are more capable of reconstructing the overall features of the velocity field and the water level distribution. However, for large-scale and complex laboratory experiments, sensing techniques have a number of shortcomings, such as the limited visual angle and object occlusion.

In laboratory experiments of urban flooding, the most common and accessible method to produce an urban flooding process is to provide an upstream runoff, including the discharge hydrograph resulting from a dam-breach event. Soares-Frazão and Zech (2007) and Aureli et al. (2015) investigated the performance of an isolated building subject to a dam-break flood event, and they conducted detailed measurements on the variation in flow pattern around the building. Further experimental studies on the flood inundation processes in idealized urban areas were conducted by Testa et al. (2007), Soares-Frazão and Zech (2008), and LaRocque et al. (2013). In these studies, it was found that the key flood characteristics, such as flow path, velocity field and water depth distribution, can be strongly influenced by the complex street layout of an urban area. The layout of a city is organized based on streets, and the natural topography is usually blocked by buildings and greenbelts. Therefore, urban streets become the main flow paths during flooding events (Mignot et al., 2006, 2013; Lee et al., 2016; Chen et al., 2018). Instead of focusing only on the pattern of surface flow, some researchers have investigated the flow exchange between surface runoff and underground pipe flow, via street inlets and manholes etc. (Noh et al., 2016; Rubinato et al., 2017; Martins et al., 2018). Previous laboratory experiments of urban flooding with sewer systems have focused on the hydraulic efficiency of street inlets (Gómez et al., 2011, 2013; Rubinato et al., 2017) and the interaction between surface runoff and sewer pipe flow (Bazin et al., 2014; Fraga et al., 2017), as well as sediment and pollutant transport during rainfall events (Naves et al., 2020). Most of the existing urban flood experiments reported in the literature for real street layouts and underground sewer systems have mainly concentrated on studying steady-state and gradually varying flow patterns, with few studies investigating unsteady flood inundation processes.

In addition to laboratory studies, numerical modelling nowadays provides the main tool used to predict the inundation extent of urban floods and has become the key tool to plan for disaster prevention and to undertake scientific investigations. Accurate modelling of real urban flood events needs to deal with irregular topographies, capture wet and dry fronts, and provide accurate predictions of transcritical flood events. Among the existing numerical models of urban flooding, the shallow water equations (SWEs) are solved within these models, achieving a balance between model accuracy and computational efficiency. A solution of the SWEs, based on the Godunov-type finite volume method, can satisfy the hyperbolic nature of the SWEs and capture discontinuities in the flow field, such as those characteristic hydraulic jumps. Therefore, this method is now one of the most popular numerical schemes used for modelling extreme flood events. Ghostine et al. (2009) adopted two different SWEs models and the more sophisticated model of FLUENT to simulate supercritical flows at street junctions, with the results indicating that the second-order SWEs model is capable of predicting the complex flow patterns occurring during urban flood events.

The increase of impervious surfaces in urban regions generally reduces the infiltration rate and causes higher surface runoff, which then leads to higher flood risks in these areas (Shao et al., 2019; Ferreira et al., 2019). In this situation, sewer systems act as the main infrastructure to drain away the surface runoff during extreme rainfall events. Many dual-drainage models have been developed to achieve simultaneous simulation of the complex processes, involving both ground surface flow and underground pipe flow (Leandro et al., 2009; Seyoum et al., 2012; Jang et al., 2018). In most of the dual-drainage models, the surface flow is calculated by solving the 2D SWEs, while the sewer flow is simulated by solving the 1D pipe flow equations. The transition of flow regime in sewer pipes is captured by adopting additional techniques, such as the Preissmann slot approach (PSA) and the two-component pressure approach (TPA) (Vasconcelos et al., 2006; Sanders and Bradford, 2011; Li et al., 2020). The drainage discharge between the ground surface and drainage pipes can be calculated using weir and/or orifice formulae (Rubinato et al., 2018). However, most of the inlet capacity formulae are derived from steady-state experiments (Gómez et al., 2011, 2013; Lee et al., 2012), and the application of these formulae in simulating highly unsteady urban flood events is a potential source of key uncertainties.

The current study is organized into five parts. Section 2 describes the experimental facility and the corresponding measurement procedure, together with the numerical modeling framework. Section 3 reports the results obtained from laboratory experiments and numerical modelling simulations, with the main impacts on the flood inundation processes being the initial water depth, different street layouts, and the urban sewer system. Section 4 presents the discussion about the importance of mesh resolution on the numerical simulations and the performance of the existing discharge capacity formulae in the dual drainage modeling. The conclusions are then given in Section 5.

2 Methods

Investigations into flood inundation processes over an idealized urban street were performed in the current study, using both generalised laboratory experiments and numerical modelling. The inundation characteristics of urban flooding over a typical urban street were measured in detail, covering the variations in water depth and flow velocity at different locations. Numerical modelling was carried out using a 2D SWEs numerical model including appropriate inlet discharge capacity formulae.

2.1 Set-up of laboratory experiments

2.1.1 Layout of the laboratory model

The experiments were conducted in a large-scale laboratory flume. The flume is 20 m long, 3 m wide, 0.6 m deep, with a horizontal bed. Both the sidewalls and the flume bed are made from transparent tempering glass, to facilitate observations. As illustrated in Fig. 1a, a dam composed of two thin walls and a 1 m wide lift-gate separates the upstream part of the laboratory flume, representing a reservoir zone. Downstream of the gate, the physical model has the layout of a real urban street. Various infrastructures are included in the model, including a road, buildings, greenbelt sections, sidewalks and an underground sewer system. The physical model was designed according to the law of Froude similarity, with a scale of one tenth to the modelled real-world scenario.

Insert Fig. 1

Each building in this study is 0.8 m long, 0.4 m wide, and 0.5 m high, designed according to the size of a widely used house in China. The model main road and sidewalk have a width of 1.2 m and 0.3 m, respectively. In addition, the model sidewalk level is 1 cm higher than the level of the model road. Ten street inlets are distributed along the left and right sides of the road (viewing downstream), with a spacing of 2 m between two consecutive street inlets. In order to describe the location of measurement points and buildings, a plane cartesian coordinate system is set up in this physical model. The origin of the axis is located at the lower-left corner of Fig. 1a (viewing downstream), with the positive *x*-axis direction facing downstream and along the left side of the flume. The exact coordinates of water level gauges and the centroid of two upstream buildings are given in Table 1. The model has a free overflow at the end and the downstream boundary can therefore be treated as an open boundary in the numerical model.

Insert Table 1

As shown in Fig. 1b, the model has a two-layer structure, and the underground sewer system is linked to the road surface via street inlets. The street inlets used in this study have a rectangular plan view, with a size of 10 cm × 20 cm, and the void ratio of the inlet grate is 28% (Fig. 1c). Both the side tubes and main pipes are made from acrylic pipes, with the corresponding inner diameters being 2.2 and 20.0 cm. A side tube is connected to a rain box with the size of 200×100×150 mm. The main sewer pipe has a longitudinal slope of 2/1000, and the upstream and downstream ends of the pipe are linked with a laboratory pump and a water tower respectively, to control the corresponding boundary conditions. Due to the water head difference along the sewer system, the overland flow drains from the ground surface to the main pipe through the street inlets. As the dam-break flow is very intense and highly unsteady, the exchange discharge through the street inlets into the sewer network also varies significantly, which makes the downstream water depth in the main pipe hard to control. In order to eliminate the uncertainties caused by the downstream boundary, the gate of the water tower remained open during the experiments. Accordingly, the downstream end of the main pipe would be treated as an open boundary. Besides, the upstream discharge of the main pipe was zero in all the cases reported herein, and the upstream boundary of the main pipe would be treated as a solid wall boundary condition.

2.1.2 Experimental procedure

At the start of each experiment, a pump was first used to fill the upstream reservoir from the laboratory water tank. After the water level in the reservoir was still, the experiment was commenced by lifting the gate quickly. It is known that dam failure is a very rapid process, and the time taken in lifting the gate has a strong influence on the corresponding experimental results. Lauber and Hager (1998) proposed a gate opening criteria for the maximum gate opening time to minimize the errors caused by the gate opening process. von Hafen et al. (2019) used a smoothed particle hydrodynamics (SPH) model to evaluate this criterion, with the results indicating that the Lauber and Hager gate opening criterion leads to an error of less than 1%, as compared with instantaneously opening the gate. In this study, a high-speed camera was used to record the gate opening time, which can guarantee that the Lauber and Hager criterion was fully satisfied.

Many unforeseen factors affect the flood inundation processes, and it is therefore impossible to obtain exactly the same results between identical experimental runs. Therefore, each experimental run was carried out at least twice to reduce the influence of unforeseen factors and ensure experimental repeatability as closely as possible. Table 2 presents a summary of all the experimental runs, and the current study covered 18 tests with different combinations of street structure and initial water depth. Case 1 was performed to investigate the idealized flood inundation with only the sidewalks being set up in the flume. Case 2 was intended to identify the influence of buildings on the flood inundation processes. Case 3 investigated the influence of urban greenbelts. Case 4 shortened the distance between buildings and increased the number of buildings to reveal the influence of building density. Cases 5 and 6 were used for investigating the mitigation effect of an urban drainage system. Each case was conducted using initial water depths of 10, 20, and 30 cm to reveal the relationship between flood intensity and initial water depth.

Insert Table 2

2.1.3 Flow measurements

The temporal variations in water levels were recorded at seven measurement points, using ultrasonic water level gauges. The water level gauges have a sampling frequency of 4 Hz, with a measurement accuracy of about ± 0.2 mm. The measurement points (i.e. P1, P2, P5, P6, and P7) are located along the centerline of the flume to record the flood routing characteristics. Measurement points P3 and P4 are located at the upstream and downstream side of the first building, to record the temporal variations in water levels around the first building. The flow velocities at points P2, P4, and P7 were measured using a 2D electromagnetic velocity meter. In comparison to using the acoustic doppler velocity meter (ADVM), the electromagnetic velocity meter can measure the instantaneous flow velocity in relatively shallow water depths. However, the water depth was too shallow to give detailed measurements of the velocity profiles along the vertical axis throughout the experiments. Therefore, only one point velocity was measured along the vertical direction at each measurement site, with the sensor being fixed at a height of 1.5 cm above the flume bottom. The sampling frequency of the velocity meter was set to 100 Hz to provide high-resolution results. Calibrated electromagnetic flowmeters were installed on each side tube to record the drainage discharge from the ground surface to the sewer system.

2.2 Framework of the numerical model

2.2.1 2D shallow water equations

Mathematical models are essential tools for simulating and evaluating urban flood inundation processes. Apart from complicated and computationally expensive three-dimensional models, 2D SWEs models achieve a good balance between model accuracy and computational efficiency. Therefore, SWEs models are widely used to simulate urban floods, with complex water depth distributions and velocity patterns. In this study, a 2D model is adopted, based on the finite volume method used to solve the SWEs (Xia et al., 2011). The governing equations of the current model can be written in the following conservative form:

$$\frac{\partial \mathbf{U}}{\partial t}+\frac{\partial \mathbf{F}(\mathbf{U})}{\partial x}+\frac{\partial \mathbf{G}(\mathbf{U})}{\partial y}=\mathbf{S} \tag{1}$$

where the vector of conserved variables:

$$\mathbf{U}=(h, hu, hv)^T \tag{2}$$

where h is the water depth; and u and v are the depth-averaged velocity components in the x- and y-coordinate directions. The flux vectors of these conserved variables are:

$$\mathbf{F}=(hu, hu^2+\tfrac{1}{2}gh^2, huv)^T;\quad \mathbf{G}=(hv, huv, hv^2+\tfrac{1}{2}gh^2)^T \tag{3}$$

The source term, including the bed slope, friction stress and drainage discharge, can be expressed by:

$$\mathbf{S}=(-q_L, gh(S_{0x}-S_{fx}), gh(S_{0y}-S_{fy}))^T \tag{4}$$

where q_L is the drainage discharge per unit area; and the bed slope terms S_{0x} and S_{0y} account for the variation of the terrain elevation z_b (m) in the x and y directions, as given by:

$$S_{0x}=-\partial z_b/\partial x;\, S_{0y}=-\partial z_b/\partial y \tag{5}$$

The bed friction terms S_{fx} and S_{fy} in the x and y directions can be formulated respectively as follows:

$$S_{fx}=n^2u\sqrt{u^2+v^2}/h^{4/3};\quad S_{fy}=n^2v\sqrt{u^2+v^2}/h^{4/3} \tag{6}$$

where n is the Manning roughness coefficient (s.m$^{-1/3}$).

2.2.2 Discharge capacity formulae for street inlets

As the major interconnection between the ground surface and the underground sewer system, street inlets play an important role in flood mitigation in urban areas. Using accurate discharge capacity formulae for street inlets is crucial to the improvement of the prediction accuracy of a numerical model. In this study, two kinds of inlet discharge capacity formulae were selected for comparison and evaluation, including the most frequently used weir and orifice formulae and the unified discharge capacity formula. Details of each approach are given below:

(i) Weir and orifice formulae for discharge capacity of street inlets

The sketch of the drainage between surface runoff and sewer pipe flow is shown in Fig. 2. In general, the drainage states of a street inlet can be generally divided into non-submerged and submerged conditions, which are governed respectively by the weir and orifice formulae. Weir and orifice formulae are the most widely accepted formulae for calculating the exchange discharge through manholes and street inlets (Noh et al., 2016; Fraga et al., 2017). According to the hydraulic status of street inlets, the exchange discharge from the surface to the rain box (Q_i) can be determined as follows:

$$Q_i = \begin{cases} C_{iw} \times \frac{2}{3} \times L\sqrt{2g}(h_{ti})^{3/2} & \text{Non-submerged} \\ C_{io} \times A_i\sqrt{2gh_{ti}} & \text{Submerged} \end{cases} \tag{7}$$

where h_{ti} is the total hydraulic head, and $h_{ti} = h_s + u_i^2/2g$; h_s is the surface water depth; u_i is the incoming surface flow velocity; A_i is the area of the street inlet; L is the perimeter of the street inlet; and C_{iw} and C_{io} are the corresponding empirical coefficients for the weir and orifice formulae.

Besides the flow exchange through inlet grates, the discharge capacity of side tubes is equally important. The formula for calculating the discharge from the rain box to the main pipe (Q_s) is almost the same as Eq. (7b), as given by:

$$Q_s = C_{so} \times A_s\sqrt{2g(h_{ts})} \tag{8}$$

where $h_{ts}=h_{sp}-h_{pm}-h_{sb}+h_b$ if the rain box is ventilated, and $h_{ts}=h_{ti}+h_{sp}-h_{pm}-h_{sb}+h_b$ if the rain box is pressurised; h_{sp} is the height between the ground surface and the bottom of the main pipe; $h_{pm} = \max(h_p, d_p/2)$; h_p is the water head in the main pipe; h_{sb} is the height between the ground surface and the bottom of the rain box; h_b is the water depth in the rain box; A_s is the inner area of the side tube; and d_p is the diameter of the main pipe.

Rain boxes can store the drainage flow between the surface and the underground sewer pipe, which shortens the inundation time and mitigates the flood intensity. Consequently, it is necessary to take the water balance of the rain box into consideration, given below:

$$\frac{\partial h_b}{\partial t} = \frac{(Q_i - Q_s)}{A_b} \tag{9}$$

where A_b is the inner area of the rain box. However, some studies have been carried out without considering the influence of rain boxes (Chanson et al., 2002; Lee et al., 2012; Martins et al., 2018). One of the most significant shortcomings of these studies is that it is difficult to quantify the transition of the discharge capacity, which is closely related to the hydraulic status of the rain box. For example, the discharge capacity of the inlet grate in most cases is larger than the value of the side tube. If the rain box is pressurised, then the total capacity will be restricted by the side tube. Therefore, this simplification has a limited scope of application and is hard to adapt to the actual situations. The performance of different formulae will be discussed in the following section, in order to quantitatively reveal the uncertainties caused by different discharge capacity formulae of street inlets.

Insert Fig. 2

(ii) Unified formula for discharge capacity of street inlet

Chen et al. (2020) conducted laboratory experiments on the discharge capacity of street inlets. Based on their experimental results, it was found that the ratio of the composite velocity through the street inlet to the incoming flow velocity can be expressed by a power function of the incoming Froude number. Therefore, a unified formula for the discharge capacity of street inlets was proposed using the method of dimensional analysis. Compared with other formulae, this formula was relatively simple and can be applied to different conditions regardless of hydraulic status:

$$Q_i = a u_i A_i Fr^b \tag{10}$$

where Fr is the Froude number in front of a street inlet; and a and b are empirical coefficients.

2.2.3 Numerical solution

The finite volume method has been widely used as a reliable tool for solving the time-dependent, nonlinear, hyperbolic shallow water equations. In this model, the second-order cell-centered Roe's scheme is used, and accordingly the average values of the conserved variables are stored at the centre of each cell. The solution of the numerical flux across the cell edge is the core of the finite volume method, and the numerical flux is evaluated at the edge of two adjacent cells by means of the monotone upstream scheme for conservation laws (MUSCL) (van Leer, 1979). Based on the rotational invariance property of the SWEs, the calculation of the numerical flux can be treated as a 1D Riemann problem. Accordingly, Roe's approximate Riemann solver is used to calculate the numerical flux across the edge. An improper treatment of the source terms may cause problems such as a reverse in the flow direction and non-physical oscillations, especially under the condition of small water depths. However, these problems can be solved by reducing the numerical time step, which sometimes leads to an unacceptable computational burden. In order to improve on the numerical stability of the scheme, a semi-implicit method is adopted in this model to discretize the bed friction term:

$$\left(S_{fx}, S_{fy}\right) = \left[\left(n^2\sqrt{u^2+v^2}\,/\,h^{4/3}\right)^k (hu)^{k+1}, \left(n^2\sqrt{u^2+v^2}\,/\,h^{4/3}\right)^k (hv)^{k+1}\right] \tag{11}$$

where the superscript k denotes the time level.

2.2.4 Mesh generation

Spatial discretization of the computational domain is a precondition in any numerical model. In this study, simulations were performed on unstructured triangular meshes, and fine meshes with a 5 cm resolution were used in order to eliminate the influence of the mesh scale. As shown in Fig. 3, unstructured meshes were implemented to replicate the geometry of the model street, and the building-hole method was adopted to represent buildings by setting up holes with solid wall boundaries (Li et al., 2019). The Manning roughness coefficients for the model road and other parts of the flume were estimated to be 0.007 and 0.012 s.m$^{-1/3}$, respectively. The downstream end of the laboratory flume was specified as a free boundary, while the other boundaries were specified as solid wall boundaries.

Insert Fig. 3

3 Experimental observations and numerical simulations

3.1 General description of the experimental flood inundation processes

Visual observations indicate that the flow patterns in different cases showed several common characteristics. After the rapid removal of the reservoir gate, the water body in the reservoir collapsed, and the extreme flood event inundated through the model street, forming a mass of shock waves. Fig. 4 presents the simulated profiles of the dam-break flow for Case 2. At the initial time, the water depth in the upstream reservoir was 30 cm, and the threshold water depth for capturing the wet and dry front was set to 1 mm. After the gate was opened, the flood wave rapidly spread over the initially dry street. The numerical model predicted a surge front propagating along the downstream road, and a rarefaction wave travelled toward the upstream reservoir. When the rarefaction wave reached the reservoir boundary, it reflected back and led to an oscillation of the free surface. Due to the interaction between the buildings and the dam-break flow, the water levels around the buildings were much higher than the levels on the model road. In addition to the water depth distribution, the presence of the buildings also altered the flow path and led to changes in the flow regime, which caused the occurrence of hydraulic jumps in the flume.

Insert Fig. 4

3.2 Effect of initial water depth on the flood inundation processes

Fig. 5 indicates the temporal variations in the water level for different initial water depths for

Case 2. A progressive reduction in the water depth was recorded at the measurement point P1, located in the upstream reservoir, and a larger initial water depth led to a more significant reduction rate and also a more intense fluctuation in the water level. As shown in Fig. 5b, the water depth downstream of the gate dramatically increased at first, with the water level being characterized by a continuous decreasing trend after reaching its maximum value. The maximum water levels for the three different initial water depths were 15.0, 12.7, 4.4 cm, respectively. A rapid rise in water depth was recorded at P3 due to the reflection effect of the building.

Insert Fig. 5

Fig. 6 illustrates the processes of flow collision with the first building for Case 4 and with the initial water depth of 30 cm; this is usually referred to as the flip-thorough process (Lugni et al., 2006). When the dam-break flow reached the front wall of the building, it climbed up as a thin layer (Fig. 6c). After a very short time, the thin layer flow collapsed and overturned backwards to rejoin the incoming flow, which produced a hydraulic jump associated with intense mixing of turbulence and air. The hydraulic jump gradually moved upstream, with the dam-break flow intensity reducing (Fig. 6e and 6f). It is worth noting that the arrival times of dam-break flows, recorded at the measurement points located in the upper part of the model, were almost the same for the different experimental scenarios. However, the recorded arrival times under different initial water depths varied significantly at the measurement points located in the lower part of the model, and a larger initial water depth produced a higher flood wave speed. At P7, the arrival times of the dam-break waves were 6.99, 8.99, 15.74 s, respectively, under the initial water depths of 30, 20, 10 cm.

Insert Fig. 6

Theoretically, the velocity and kinetic energy of dam-break flows are associated with the initial water depth. In order to reveal the relationship between the initial water depth and flood intensity, flow velocity measurements were performed during the experiments. As the water depths on the left and right sides of the flume were too shallow to conduct continuous measurements, especially under small initial water depth scenarios, only the flow velocities along the flume centerline were measured. Fig. 7 shows the velocity variations at points P2, P5 and P7 located from upstream to downstream. In general, a larger initial water depth led to a higher flow velocity, especially in the lower part of the idealized street. As shown in Fig. 7a and 7c, the maximum velocities at the upstream side under all scenarios were 1.34, 1.62, 1.78 m/s, respectively, whereas the corresponding velocities at the end of the street were 0.38, 1.35, 1.60 m/s. Furthermore, another noticeable difference is that for the cases with small initial water depths, the maximum velocities of the dam-break flows decreased along the street. However, under the condition of a 30 cm initial water depth, the flow velocity first increased along the model road and then decreased. The maximum velocity at the three measurement points mentioned above was 2.11 m/s, which was located in the middle part of the street.

Insert Fig. 7

3.3 Flood inundation characteristics for different street layouts

For the case of a 30 cm initial water depth, comparisons of the water depth variations were undertaken for different street layouts. As shown in Fig. 8, there was no apparent difference in the water depth variations at P2 during the first 30 seconds. The reason for this is that the large difference between the water levels at the upstream and downstream locations led to a large flow velocity, as well as supercritical flow conditions. The flow velocity reduced with the decreasing upstream water depth, and the flow pattern was gradually transformed from a supercritical to subcritical state. Therefore, the sudden rise in the water level was recorded at P2, due to the occurrence of the hydraulic jump. As compared with those cases without buildings, the water depth at P3 was much higher, due to the effect of the building reflection. Fig. 8d highlights that the maximum water levels for different scenarios were almost the same at the downstream side of the first building. However, the flood peak time for Case 4 was delayed, reflecting the resistance effect of the urban greenbelts. Furthermore, buildings reduced the wetted cross-sectional area of the street, causing higher water depths on the model road. In conclusion, buildings caused the onset of hydraulic jumps and an increase in the water levels, therefore intensifying the impact of urban flooding disasters. However, the influences of the street layouts and greenbelt areas on the inundation processes of urban floods are relatively insignificant, and the flood inundation process over an urban street is mainly controlled by the upstream boundary condition for this situation.

Insert Fig. 8

3.4 Mitigation effect of the drainage system on the flood inundation process

In these experiments, all the street inlets were fully submerged in the first 60 seconds after the wet/dry interface reached its location. During this period, the drainage boxes, as well as the side tubes, were converted into a pressurised state, while the main drainage pipe was kept ventilated. Hence, the exchange discharge through the street inlets was related to the water head difference between the surface runoff and the pipe flow. In order to measure the drainage discharge through the street inlets, an electromagnetic flowmeter was located on each side tube. However, accurate measurements of the drainage discharge through the street inlets were challenging for such a highly unsteady flow condition. In the first few seconds, the intense air mixing in rain boxes led to complex two-phase flow patterns in the side tubes, which reduced the accuracy of the discharge hydrographs measured using the flowmeters. Furthermore, the discharge hydrographs measured through the side tubes were significantly delayed relative to the actual discharge processes through the street inlets. Therefore, in addition to the variation in the drainage discharge, the occurrence time when the flow regime in the side tubes converted from ventilated to pressurised was also recorded, to provide the start time of the effective discharge measurement. The average drainage discharges for Cases 5 and 6 over the initial 40 s period through inlet1 are presented in Table 3, with these results providing an approximate assessment basis for the model accuracy.

Fig. 9 illustrates the influence of the drainage system on the variation in the surface water depth. As most of the street inlets were located at the middle and lower sides of the street, the reduction in the water depth became more apparent from the upper to the lower part of the flume. The sewer system not only reduced the surface water depth, but also had a significant influence on the velocity of the dam break flow. The flow depths at P7 were 1.81 cm and 2.17 cm, respectively, under scenarios with and without the drainage system after the gate opening of 40 seconds, with the corresponding wave arrival times of 16.21 s and 14.75 s respectively. In conclusion, street inlets were found to reduce both the water depth and flood wave velocity, which significantly shortened the flood inundation time.

Insert Fig. 9

Insert Table 3

3.5 Comparisons between numerical simulations and experimental observations

Fig. 10 illustrates a comparison of the simulated and experimentally observed variations in the water depth hydrographs at different measurement points for Case 2. In general, the SWEs model used in this study has accurately reproduced the water level variations throughout the whole process, with relative errors of less than 5% at most of the measurement points. However, there were some visible differences between the simulated results and the observed data at the measurement points P2 and P3, and the simulated flood peak levels were noticeably lower than the observed values, with the relative errors being 5.46% and 35.7%, respectively (Fig. 10b and 10c). At these locations, the dam-break flow was characterized by pronounced three-dimensional properties, which cannot be described by the traditional 2D SWEs. When the dam-break wave impinged on these buildings, the collision between the reflection wave and the incoming flow caused violent turbulence and air entertainment, and the current SWEs model is not capable of predicting such complex 3D flow patterns. Furthermore, it should be noted that the free-surface oscillations were not successfully reproduced, and the simulated water level hydrograph was smoother than the observed one. In addition to water depth variations, the model results show some errors in capturing the wet/dry front, and the simulated arrival time of the dam-break wave at P6 was delayed relative to the observed value.

Insert Fig. 10

3.6 Numerical modelling with the inclusion of street inlets

In this section, the discharge data measured using the electromagnetic flowmeters were directly used to provide the drainage discharges through the street inlets. The computational meshes within each street inlet were identified as exchange cells, where the mass source term q_L in Eq. (1) is non-zero. The exchange discharge within a mesh (Q_m) is calculated using the formula:

$$Q_m = \frac{Q_i \times A_m}{A_i} \tag{12}$$

where the subscript *m* represents the index of computation cells; and A_m is the area of the mesh.

It should be noted that the influence of a street inlet in previous studies reported in the literature (Bazin et al., 2014; Noh et al., 2016; Rubinato et al., 2017) is usually represented by a mass source point, through which the surface runoff is added (or subtracted) to the underground sewer flow. However, street inlets not only affect the mass term but also directly influence the momentum balance of the surface runoff. Many researchers have investigated the flow velocity fields, turbulence characteristics, and local energy losses in manholes and sewer junctions (Rubinato et al., 2018; Kim et al., 2018). However, investigations into the influence of a sewer system on the surface runoff are seldom reported. Further investigations into the local energy loss and velocity field variations caused by street inlets should be carried out in the future to improve the predictive accuracy of the numerical model. The temporal evolutions of the velocity field and water level distribution around a street inlet are illustrated in Fig. 11. After the gate opening of 3 seconds, the wet/dry interface reached the location of the first street inlet. During the first 20 seconds, the positions of the maximum velocity and minimum water depth within a street inlet were located at the downstream side, due to the high velocity of the dam-break flow (Fig. 11 a-d). As the velocity of the dam-break flow decreased, the positions of the maximum flow velocity and minimum water depth gradually moved upstream (Fig. 11e, f). The water level around a street inlet was significantly lower than the value in the adjacent area, and street inlets also influenced the local velocity fields, with the velocity vector in the adjacent area pointing slightly towards the centerline of the street inlet.

Insert Fig. 11

4 Discussion

4.1 Effect of mesh resolution

Mesh generation and resolution are critical in terms of acquiring accurate numerical predictions in computational model studies. Variations in the mesh resolution can lead to different simulated results and computational requirements. A finer mesh resolution benefits the representation of a computational domain, particularly for complex bathymetries and solid structures etc., and also provides more accurate predictions of small-scale hydraulic features. However, the use of small meshes also reduces the computational efficiency in terms of increasing the mesh amount and shortening the numerical time step (Horritt et al., 2006). In the current study, indicators such as the Nash-Sutcliffe efficiency (NSE) and the root mean square error (RMSE) are used to evaluate the model performance using different mesh resolutions. The Nash-Sutcliffe efficiency coefficient (NSE) is one of the most frequently used evaluation criterion in hydrodynamic modeling and is given by:

$$\mathrm{NSE} = 1 - \frac{\sum_{i=1}^{AMT} (y_i - \hat{y}_i)^2}{\sum_{i=1}^{AMT} (y_i - \bar{y})^2} \tag{13}$$

where AMT is the amount of data points; y_i is the observed value (in this section y is the water depth); $\hat{y}_i$ is the simulated value; and $\bar{y}$ is the average value of the observed data.

The root mean square error (RMSE) is another widely used criterion, which provides a valuable general-purpose error metric parameter for comparing numerical model predictions and is given by:

$$\mathrm{RMSE} = \sqrt{\frac{1}{AMT} \sum_{i=1}^{AMT} (y_i - \hat{y}_i)^2} \tag{14}$$

In order to assess the relationship between the mesh resolution and computational results, numerical simulations were conducted using meshes with resolutions of 5, 10, and 20 cm. Fig. 12 illustrates the variations in the NSE and RMSE parameters for the different mesh resolutions.

Generally, the numerical model accurately reproduced the water level variations at most of the measurement points, with the NSE values being greater than 0.9 and the RMSE values less than 1×10^{-3}. As expected, the results using the 5 cm mesh resolution gives the best performance. In addition, the model-performance difference between the mesh sizes of 5 cm and 10 cm is smaller than the difference between the mesh sizes of 10 cm and 20 cm, suggesting that further refinement of the computational mesh would only slightly improve the computational results. The model performance evaluation discussed above was also conducted for different initial water depths, and it was clear that as comparison with the larger initial water depth scenarios, the small initial water depth scenarios were more sensitive to the mesh resolution. Furthermore, the computational times differ significantly between the different mesh resolutions. The mesh resolutions of 5, 10, and 20 cm corresponded to 52516, 13684, 3440 cells, respectively, and led to the corresponding computational times of 22, 8, and 2 minutes. Based on the above analysis, it was deemed necessary to select the appropriate mesh size to balance the computational efficiency with accuracy in the numerical modelling.

Insert Fig. 12

4.2 Comparison of different discharge capacity formulae in the numerical model

Street inlets control the interaction between surface runoff and underground pipe flow, and therefore, these inlets directly affect the extent of urban flood inundation. The calculation of drainage discharge through street inlets is one of the most critical factors in simulating urban flooding. Most of the existing discharge capacity formulae for street inlets are derived from laboratory experiments under steady-state flow conditions. In order to test the applicability of these formulae in simulating highly unsteady urban flood events, different discharge capacity formulae for street inlets were integrated into the 2D SWEs model based on the finite volume method, and the integrated model was used to reproduce the flood inundation processes, as well as the flow exchange through the street inlets. In this study only the following formulations were selected for comparison and evaluation in the model studies, including: (i) the weir and orifice formulae, which considered the influence of the rain box, termed as WOFR (i.e. Eqs. (7) - (9)); (ii) the simplified weir and orifice formulae, termed as SWOF, which only included the discharge capacity of the inlet grates (i.e. Eq. (7)); and (iii) the unified discharge capacity formula, termed as UF (i.e. Eq. (10)). The key parameters in these discharge capacity formulae were governed by many factors, such as the shape and void ratio of the inlet grates, the size of the rain boxes, and also the geometry of side tubes. Therefore, parameter calibration was essential in the absence of a generally accepted standard for the discharge coefficients for different types of inlets. In this study, the coefficients were calibrated using the trial and error method based on numerical tests, and the calibrated values are presented in Fig. 13a. For the weir and orifice formulae, many researchers have suggested to use the ratio of the total surface water head to the thickness of inlet grate, as the criteria to distinguish the weir and orifice drainage status (Chanson et al., 2002; Noh et al., 2016). Based on experimental observations, as well as numerical simulations, $h_{ti}/w = 0.2$ was used as the criterion to distinguish the weir and orifice flows, where w is the width of the inlet grate.

Fig. 13 presents the results using different discharge capacity formulae. As shown in Fig. 13a, the SWEs model, including different discharge capacity formulae, can accurately reproduce the water level variation with careful calibration of the model parameters. About 0.23 m^3 of the surface runoff was drained through the street inlets in the first 40 seconds, accounting for as much as 17% of the total flow volume. The simulated discharge hydrographs drained through inlet5, using different discharge capacity formulae, are shown in Fig. 13b. The results obtained using the WOFR showed a significant difference as comparison with the results obtained using the SWOF and UF. In the first few seconds, the rain box was ventilated, and the street inlet showed a larger drainage efficiency. After the rain box was pressurised, the drainage efficiency was mainly determined by the discharge capacity of the side tube, and the drainage discharge was relatively small. This phenomenon agreed well with the fact that the discharge capacity for the inlet grate was larger than the capacity of the side tube. The drainage discharge difference was 1.4 L/s between the cases for the ventilated and pressurised rain boxes, indicating a high sensitivity to the conversion of the hydraulic status within the rain box. The results from the UF and SWOF showed similar characteristics. The drainage discharge gradually reduced after reaching the maximum value, which was 0.80 and 0.82 L/s, respectively. As the SWOF lacks inclusion of the influence of the side tubes, parameter modifications were required to provide an indirect reflection. The calibrated inlet orifice coefficient w_{is} was set to 0.12 for the WOFR, while the value was set to 0.03 for the SWOF.

The simulated drainage discharges through the different street inlets for the WOFR and UF are presented in Figs. 13c and 13d, respectively. According to the structure of the UF, the exchange discharge is directly related to the surface water depth and the flow velocity, which decreases along the street. Therefore, the street inlets located at the upstream side of the flume had a larger drainage efficiency than the other street inlets. However, for the WOFR, the discharge capacity of a street inlet was determined by the water head difference between the surface runoff and the underground sewer flow after the rain box was pressurised. As the water head of surface runoff was relatively small compared to the height between the main pipe and the road surface, the drainage efficiency varied slightly from the upper and lower part of the flume.

In general, the integrated model can accurately simulate the variation in the surface water depth when the impacts of street inlets and sewer pipes are included. However, the weir and orifice formulae provide flexibility in terms of characterizing the structures and physical processes of different sewer systems and are more capable of capturing the transition of the inlet drainage status. However, the UF and SWOF lack consideration of some critical physical processes. Therefore, modifications of the empirical parameters are required to provide an approximate solution. This approximation is challenging to meet the actual requirements for accurate predictions and may therefore introduce some additional uncertainties in the numerical model predictions.

Insert Fig. 13

5 Conclusions

In the current study, an idealized laboratory model of a typical urban street with a sewer system underneath, was set-up to acquire a better understanding of the flood inundation processes occurring in an urban environment. In order to reflect the influence of different street layouts and infrastructures on the flood processes, detailed water level evolutions and flow velocity variations were measured at several predetermined points for different experimental scenarios. In addition to the detailed flume experiments, numerical model simulations were also conducted using a 2D SWEs model, with different discharge capacity formulae for street inlets being included in the model, in order to replicate the flood inundation processes and the interaction between the surface runoff and sewer system discharge. The conclusions from the laboratory experiments and the numerical model simulations can be summarised as follows:

(i) Based on the analysis of the experimental results, it was found that buildings would reduce the wetted cross-sectional area of flow and therefore increase the water levels on the road. Compared with the street layout, the upstream boundary condition and the sewer system capacity have a more significant influence on the highly unsteady urban flood inundation processes. A larger building density and the arrangement of greenbelt areas can slightly increase the water depth on the road. The use of urban sewer systems can reduce both the water depth and the flow velocity and, therefore, effectively alleviate the disaster of urban flooding and waterlogging.

(ii) The 2D SWEs model used in this study was shown to be capable of simulating the urban flood inundation processes, with the NSE values being larger than 0.9 and the RMSE values being less than 0.15×10^{-3} at all the measurement points. Based on the simulated results, it was found that for a 10 cm initial water depth, about 17% of the total volume was drained from the surface to the sewer system during the first 40 seconds. The street inlets not only reduced the runoff water depth, but also changed the local velocity field, and the position of the maximum velocity and minimum water depth around a street inlet, with these parameters varying with the incoming flow intensity.

(iii) A sensitive analysis indicated that a fine resolution mesh improved the model performance, in terms of accuracy. However, further refinements to the mesh were only slight, but the numerical model simulations led to much more computational time being required after reaching a certain mesh resolution. This meant that real-time, long-term and large-scale simulations were unrealistic. Furthermore, the choice of the discharge capacity formulae for representing street inlets plays an essential role in improving the accuracy of dual drainage modeling. The weir and orifice formulae, with the inclusion of the impact of the rain box, were more accurate in capturing the transition of the drainage discharge through street inlets and showed the best performance in this study.

Acknowledgments

This work was funded by the National Natural Science Foundation of China (Grant Nos. 51725902, 41890820); the Royal Academy of Engineering through the Urban Flooding Research Policy Impact Programme (Grant No. UUFRIP\100031); and the Newton Advanced Fellowships from the NSFC and the UK Royal Society (Grant Nos. 52061130219; NAF\R1\201156).

References

[1] Aureli, F., Dazzi, S., Maranzoni, A., Mignosa, P. and Vacondio, R., 2015. Experimental and numerical evaluation of the force due to the impact of a dam-break wave on a structure. Advances in Water Resources, 76: 29-42.

[2] Bazin, P., Nakagawa, H., Kawaike, K., Paquier, A. and Mignot, E., 2014. Modeling flow exchanges between a street and an underground drainage pipe during urban floods. Journal of Hydraulic Engineering, 140: 04014051.

[3] Bennett, N.D. et al., 2013. Characterising performance of environmental models. Environmental Modelling & Software, 40(2013): 1-20.

[4] Chanson, H., Aoki, S. and Maruyama, M., 2002. Unsteady two-dimensional orifice flow: a large-size experimental investigation. Journal of Hydraulic Research, 40(1): 63-71.

[5] Chen, B., Krajewski, W.F., Goska, R. and Young, N., 2017. Using LiDAR surveys to document floods: A case study of the 2008 Iowa flood. Journal of Hydrology, 553: 338-349.

[6] Chen, Q., Xia JQ., Dong B., 2020. Experimental study on discharge capacity of street inlet in urban flooding. Advances in Water Science, 2020,31(01):10-17. (In Chinese) doi: 10.14042/j.cnki.32.1309.2020.01.002

[7] Chen, S. et al., 2018. Variance based sensitivity analysis of 1D and 2D hydraulic models: An experimental urban flood case. Environmental Modelling & Software, 109: 167-181.

[8] Cheng, X., Han, G., Zhao, Y. and Li, L., 2019. Evaluating Social Media Response to Urban Flood Disaster: Case Study on an East Asian City (Wuhan, China). Sustainability, 11(19): 5330. doi: 10.3390/su11195330.

[9] Ferreira, C.S.S. et al., 2019. Impacts of distinct spatial arrangements of impervious surfaces on runoff and sediment fluxes from laboratory experiments. Anthropocene, 28(2019): 100219.

[10] Fraga, I., Cea, L. and Puertas, J., 2017. Validation of a 1D-2D dual drainage model under unsteady part-full and surcharged sewer conditions. Urban Water Journal, 14(1): 74-84.

[11] Ghostine, R. et al., 2009. Simulation of supercritical flow in crossroads: Confrontation of a 2D and 3D numerical approaches to experimental results. Computers & Fluids, 38(2): 425-432.

[12] Gómez, M. and Russo, B., 2011. Methodology to estimate hydraulic efficiency of drain inlets. Proceedings of the Institution of Civil Engineers - Water Management, 164(2): 81-90.

[13] Gómez, M., Rabasseda, G.H. and Russo, B., 2013. Experimental campaign to determine grated inlet clogging factors

in an urban catchment of Barcelona. Urban Water Journal, 10(1): 50-61.

[14] Horritt, M.S., Bates, P.D. and Mattinson, M.J., 2006. Effects of mesh resolution and topographic representation in 2D finite volume models of shallow water fluvial flow. Journal of Hydrology, 329(1-2): 306-314.

[15] Jang, J., Chang, T. and Chen, W., 2018. Effect of inlet modelling on surface drainage in coupled urban flood simulation. Journal of Hydrology, 562: 168-180.

[16] Kim, J., Jo, J. and Yoon, S., 2018. Head Loss Reduction in Surcharged Four-Way Junction Manholes. Water, 10(12): 1741. doi: 10.3390/w10121741

[17] LaRocque, L.A., Elkholy, M., Hanif Chaudhry, M. and Imran, J., 2013. Experiments on Urban Flooding Caused by a Levee Breach. Journal of Hydraulic Engineering, 139(9): 960-973.

[18] Lauber, G. and Hager, W.H., 1998. Experiments to dambreak wave: Horizontal channel. Journal of Hydraulic Research, 36(3): 291-307.

[19] Leandro, J., Chen, A.S., Djordjević, S. and Savić, D.A., 2009. Comparison of 1D/1D and 1D/2D Coupled (Sewer/Surface) Hydraulic Models for Urban Flood Simulation. Journal of Hydraulic Engineering, 135(6): 495-504.

[20] Lee, S., Nakagawa, H., Kawaike, K. and Zhang, H., 2012. Study on Inlet Discharge Coefficient Through the Different Shapes of Storm Drains for Urban Inundation Analysis. Journal of Japan Society of Civil Engineers, 68(4): I_31-I_36.

[21] Lee, S., Nakagawa, H., Kawaike, K. and Zhang, H., 2016. Urban inundation simulation considering road network and building configurations. Journal of Flood Risk Management, 9(3): 224-233.

[22] Li, Q., Liang, Q. and Xia, X., 2020. A novel 1D-2D coupled model for hydrodynamic simulation of flows in drainage networks. Advances in Water Resources, 137: 103519.

[23] Li, Z. et al., 2019. Comparative Analysis of Building Representations in TELEMAC-2D for Flood Inundation in Idealized Urban Districts. WATER, 11(9): 1840. doi: 10.3390/w11091840

[24] Lugni, C., Brocchini, M. and Faltinsen, O.M., 2006. Wave impact loads: The role of the flip-through. Physics of Fluids, 18(12): 122101.

[25] Martínez-Aranda, S., Fernández-Pato, J., Caviedes-Voullième, D., García-Palacín, I. and García-Navarro, P., 2018. Towards transient experimental water surfaces: A new benchmark dataset for 2D shallow water solvers. Advances in Water Resources, 121: 130-149.

[26] Martins, R. et al., 2018. On the Characteristics of Velocities Fields in the Vicinity of Manhole Inlet Grates During Flood Events. Water Resources Research, 54(9): 6408-6422.

[27] Mignot, E. et al., 2013. Impact of topographic obstacles on the discharge distribution in open-channel bifurcations. Journal of Hydrology, 494: 10-19.

[28] Mignot, E., Li, X. and Dewals, B., 2019. Experimental modelling of urban flooding: A review. Journal of Hydrology, 568: 334-342.

[29] Mignot, E., Paquier, A. and Haider, S., 2006. Modeling floods in a dense urban area using 2D shallow water equations. Journal of Hydrology, 327(1-2): 186-199.

[30] Naves, J., Anta, J., Suárez, J. and Puertas, J., 2020. Hydraulic, wash-off and sediment transport experiments in a full-scale urban drainage physical model. Scientific Data. doi:10.1038/s41597-020-0384-z .

[31] Noh, S.J., Lee, S., An, H., Kawaike, K. and Nakagawa, H., 2016. Ensemble urban flood simulation in comparison with laboratory-scale experiments: Impact of interaction models for manhole, sewer pipe, and surface flow. Advances in Water Resources, 97: 25-37.

[32] Puech, C. and Raclot, D., 2002. Using geographical information systems and aerial photographs to determine water levels during floods. Hydrological Processes, 16(8): 1593-1602.

[33] Qian, C., Junqiang, X. and Boliang, D., 2020. Experimental study on discharge capacity of street inlet in urban flooding. Advances in Water Science, 31(1): 10-17.

[34] Rubinato, M. et al., 2017. Experimental calibration and validation of sewer/surface flow exchange equations in steady and unsteady flow conditions. Journal of Hydrology, 552: 421-432.

[35] Rubinato, M., Lee, S., Martins, R. and Shucksmith, J.D., 2018. Surface to sewer flow exchange through circular inlets during urban flood conditions. Journal of Hydroinformatics, 20(3): 564-576.

[36] Sanders, B.F. and Bradford, S.F., 2011. Network Implementation of the Two-Component Pressure Approach for Transient Flow in Storm Sewers. Journal of Hydraulic Engineering, 137(2): 158-172.

[37] Seyoum, S.D., Vojinovic, Z., Price, R.K. and Weesakul, S., 2012. Coupled 1D and Noninertia 2D Flood Inundation Model for Simulation of Urban Flooding. Journal of Hydraulic Engineering, 138(1): 23-34.

[38] Shao, Z., Fu, H., Li, D., Altan, O. and Cheng, T., 2019. Remote sensing monitoring of multi-scale watersheds impermeability for urban hydrological evaluation. Remote Sensing of Environment, 232(2019): 111338.

[39] Soares-Frazão, S. and Zech, Y., 2007. Experimental study of dam-break flow against an isolated obstacle. Journal of Hydraulic Research: Dam-Break Flow Experiments and Real-Case Data. A Database from the European IMPACT Research Program, 45(sup1): 27-36.

[40] Soares-Frazão, S. and Zech, Y., 2008. Dam-break flow through an idealised city. Journal of Hydraulic Research, 46(5): 648-658.

[41] Testa, G., Zuccalà, D., Alcrudo, F., Mulet, J. and Soares-Frazão, S., 2007. Flash flood flow experiment in a simplified urban district. Journal of Hydraulic Research: Dam-Break Flow Experiments and Real-Case Data. A Database from the European IMPACT Research Program, 45(sup1): 37-44.

[42] van Leer, B., 1979. Towards the ultimate conservative difference scheme. V. A second-order sequel to Godunov\"s method. Journal of Computational Physics, 32(1): 101-136.

[43] Vasconcelos, J.G., Wright, S.J. and Roe, P.L., 2006. Improved Simulation of Flow Regime Transition in Sewers: Two-Component Pressure Approach. Journal of Hydraulic Engineering, 132(6): 553-562.

[44] von Hafen, H., Goseberg, N., Stolle, J. and Nistor, I., 2019. Gate-Opening Criteria for Generating Dam-Break Waves. Journal of Hydraulic Engineering, 145(3): 04019002.

[45] Xia, J., Falconer, R.A., Lin, B. and Tan, G., 2011. Numerical assessment of flood hazard risk to people and vehicles in flash floods. Environmental Modelling & Software, 26(8): 987-998.

List of Table and Figure Captions

Table 1 Positions of water level gauges and buildings.

Table 2 Summary of experimental runs and corresponding conditions.

Table 3 Averaged drainage discharges through inlet1 for different cases. (Unit: L/s)

Fig. 1 Sketch of the physical model showing a typical urban street.

Fig. 2 Sketch of the drainage status between surface runoff and sewer pipe flow.

Fig. 3 Zoom of the mesh characterization around a street inlet.

Fig. 4 Spatial and temporal evolutions of the dam-break flow for Case 2 at different times of: (a) t=1.0 s; (b) t=2.0 s; (c) t=4.0 s; (d) t=6.0 s; (e) t=8.0 s; (f) t=10.0 s.

Fig. 5 Temporal variations in water depth at sites of: (a) P1; (b) P2; (c) P3; (d) P4; (e) P5; (f) P7.

Fig. 6 Video images showing the process of the collision between the dam-break flow and the building for Case 4, for an initial water depth of 30 cm at different times of: (a) t=0.00 s; (b) t=1.73 s; (c) t=2.10 s; (d) t=2.83 s; (e) t= 3.29 s; (f) t=4.79 s.

Fig. 7 Temporal variations in flow velocities for different initial water depths at sites of: (a) P2; (b) P5; (c) P7.

Fig. 8 Comparisons of water depth hydrographs for various street layouts at sites of: (a) P1; (b) P2; (c) P3; (d) P4; (e) P5; (f) P7.

Fig. 9 Effects of the sewer system on water depth variations for the initial water depth of 10 cm (Cases 4 and 6) at sites of: (a) P1; (b) P2; (c) P3; (d) P4; (e) P5; (f) P7.

Fig. 10 Comparisons between simulated and observed variations in the water depth hydrographs at sites of: (a) P1; (b) P2; (c) P3; (d) P4; (e) P5; (f) P6.

Fig. 11 Velocity fields and water level distributions around the first street inlet for Case 2, for a 30 cm initial water depth at different times of: (a) t=3 s; (b) t=6 s; (c) t=10 s; (d) t=20 s; (e) t=30 s; (f) t=40 s.

Fig. 12 Model performance variations for different mesh resolutions under initial water depths of: (a) 10 cm; (b) 20 cm; (c) 30 cm.

Fig. 13 Simulated hydrographs of surface water depth, drainage discharge and total drainage volume based on different discharge capacity formulae, showing: (a) surface water depth variations at P5; (b) simulated and measured drainage discharges through inlet5; and (c, d) drainage discharge variations along the street direction and total drainage volume obtained using the WOFR and UF, respectively.

Table 1 Positions of water level gauges and buildings.

Positions	P1	P2	P3	P4	P5	P6	P7	Building 1	Building 2
x (m)	3.7	4.9	7.0	8.0	9.5	13.5	16.2	7.5	7.5
y (m)	1.5	1.5	0.4	0.5	1.5	1.5	1.5	0.4	2.6

Table 2 Summary of experimental runs and corresponding conditions.

Case	Number of buildings	Building spacing(m)	Greenbelt	Sewer system	Initial water depth (cm)
1	×	×	×	×	10/20/30
2	12	0.80	×	×	10/20/30
3	12	0.80	√	×	10/20/30
4	16	0.55	×	×	10/20/30
5	12	0.80	×	√	10/20/30
6	16	0.55	×	√	10/20/30

Table 3 Averaged drainage discharges through inlet1 for different cases. (Unit: L/s)

Q_i	30 cm	20 cm	10 cm
Case 5	0.69	0.68	0.67
Case 6	0.71	0.69	0.68

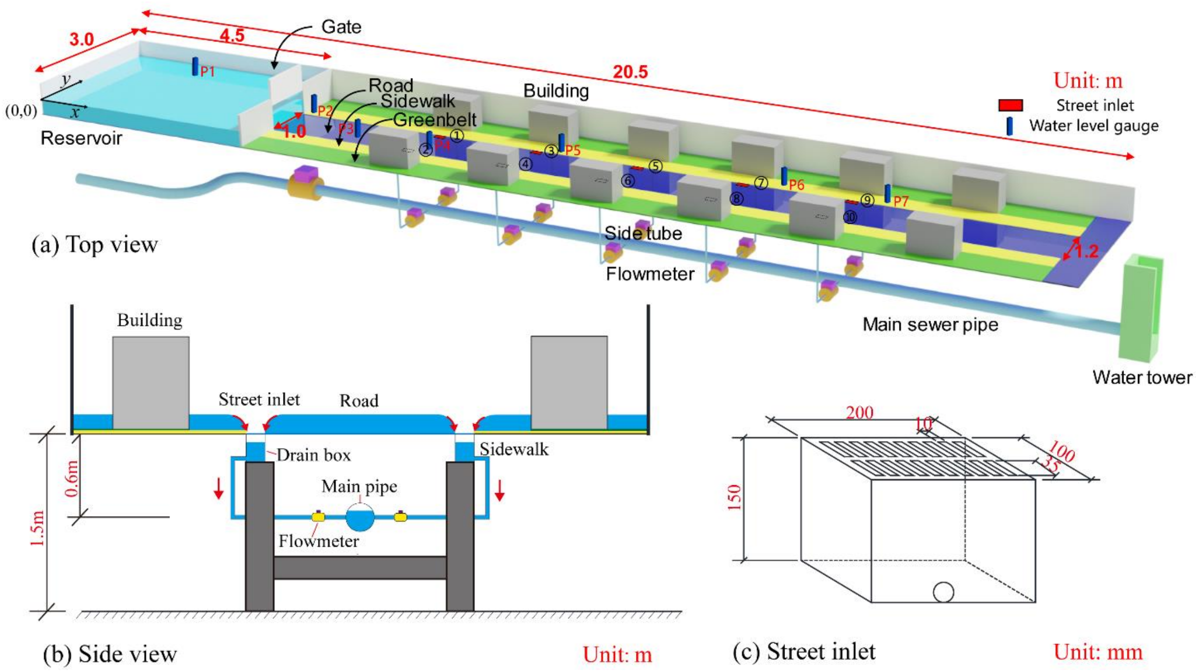

Fig. 1 Sketch of the physical model showing a typical urban street.

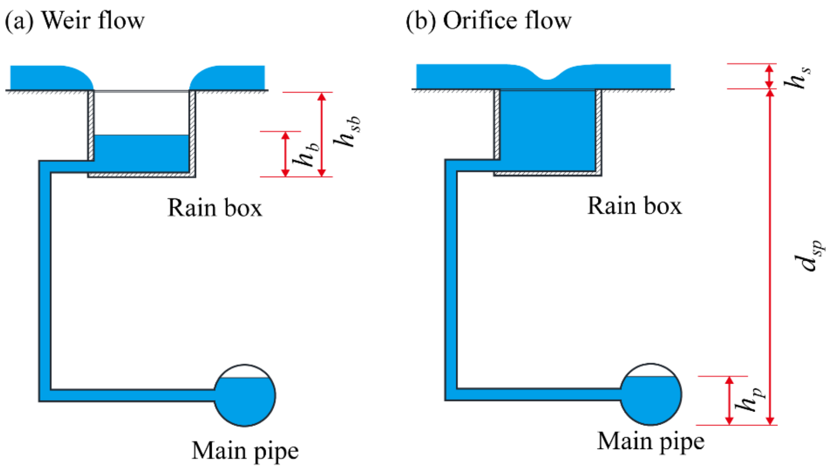

Fig.2 Sketch of the drainage status between surface runoff and sewer pipe flow.

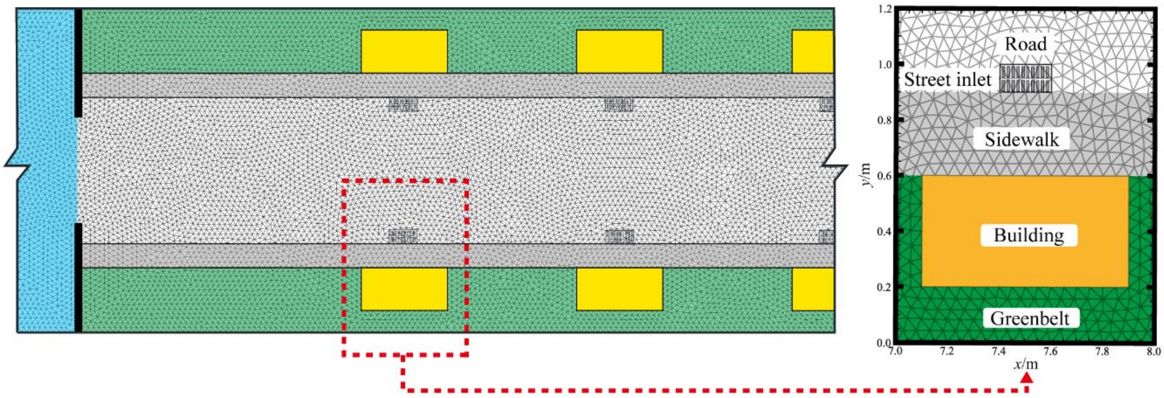

Fig. 3 Zoom of the mesh characterization around a street inlet.

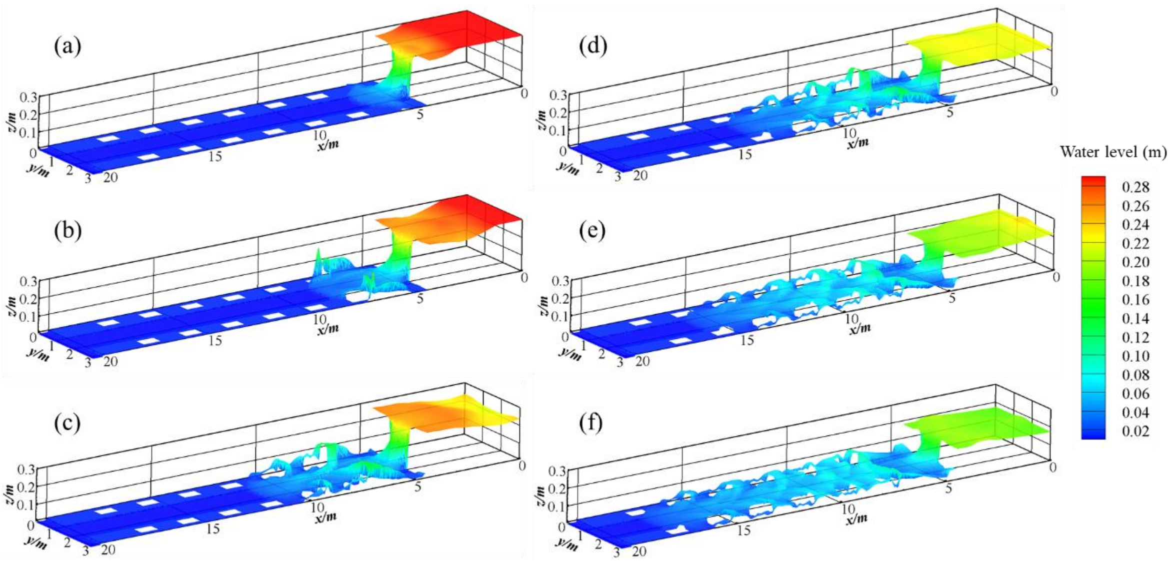

Fig. 4 Spatial and temporal evolutions of the dam-break flow for Case 2 at different times of: (a) t= 1.0 s; (b) t=2.0 s; (c) t=4.0 s; (d) t=6.0 s; (e) t=8.0 s; (f) t=10.0 s.

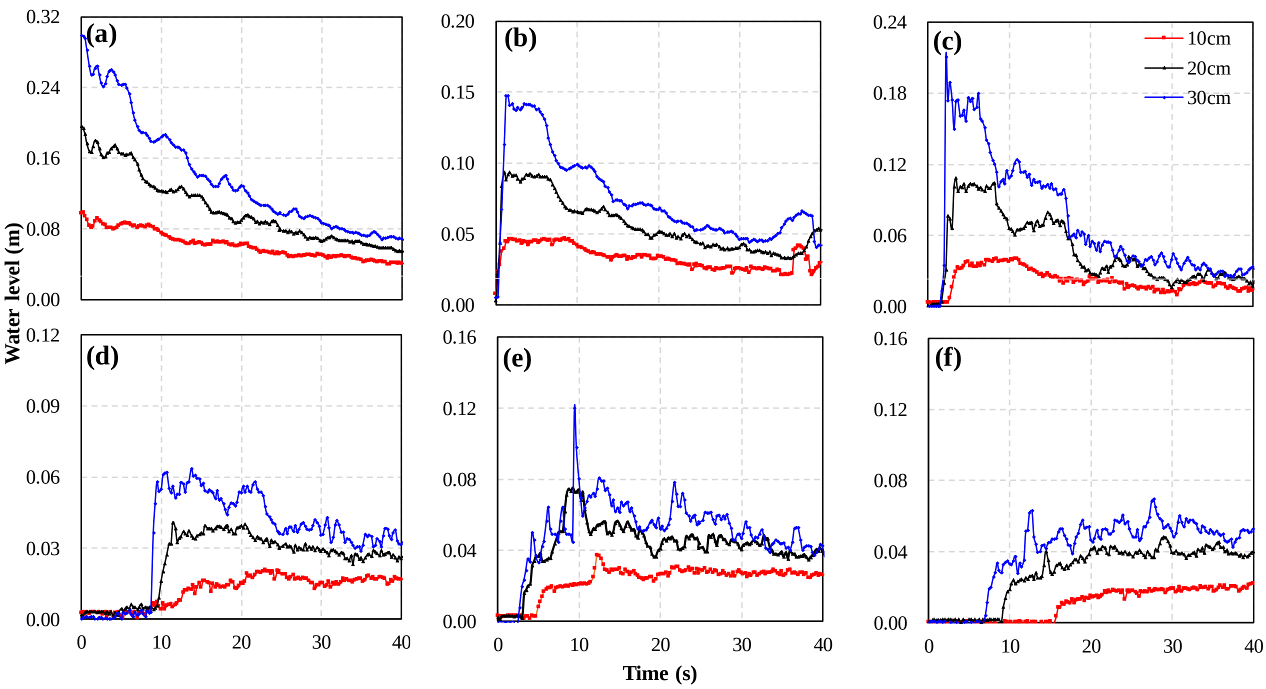

Fig. 5 Temporal variations in water depth at sites of: (a) P1; (b) P2; (c) P3; (d) P4; (e) P5; (f) P7.

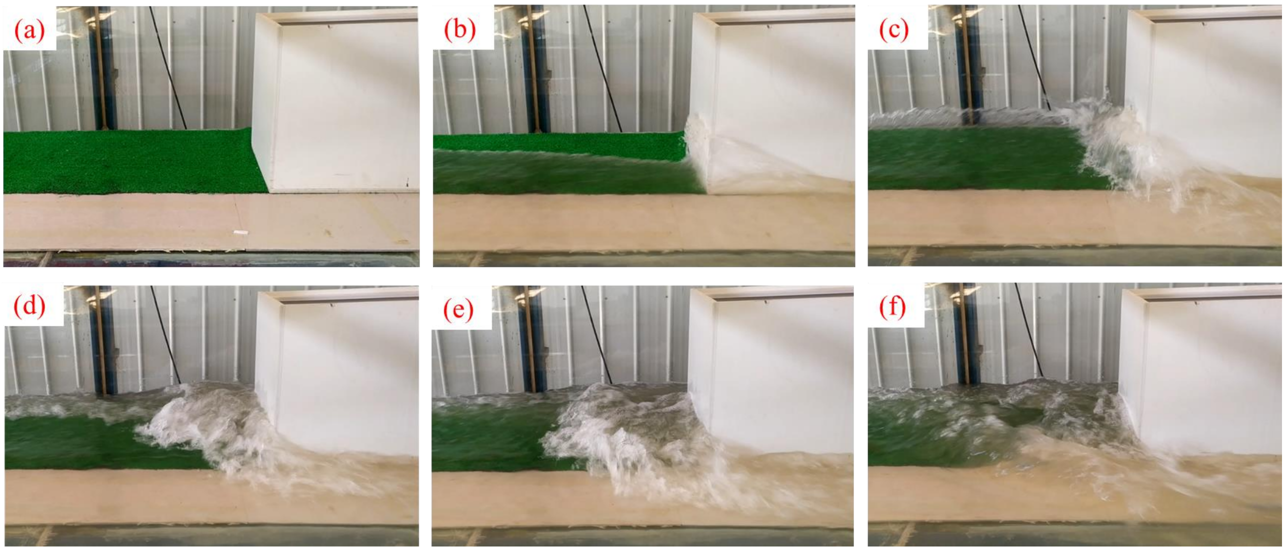

Fig. 6 Video images showing the processes of the collision between the dam-break flow and the building for Case 4, for an initial water depth of 30 cm at different times of: (a) t=0.00 s; (b) t=1.73 s; (c) t=2.10 s; (d) t=2.83 s; (e) t= 3.29 s; (f) t=4.79 s.

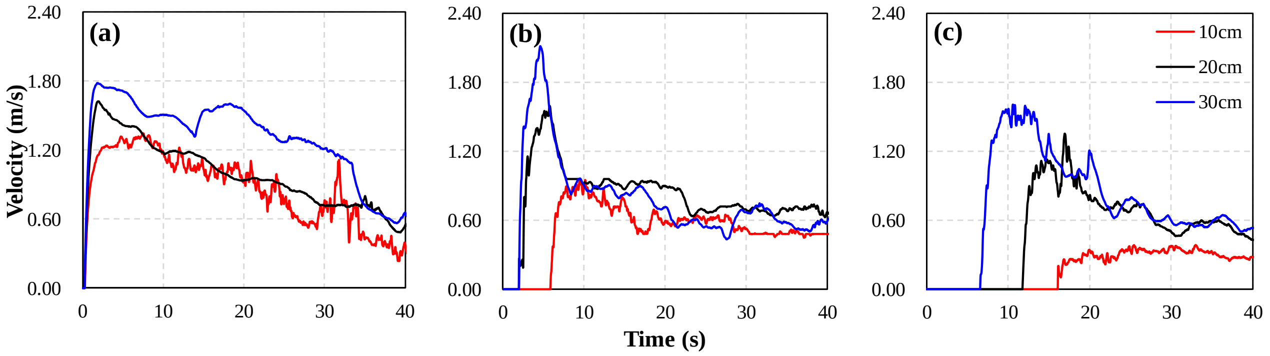

Figure 7 Temporal variations in flow velocities for different initial water depths at sites of: (a) P2; (b) P5; (c) P7.

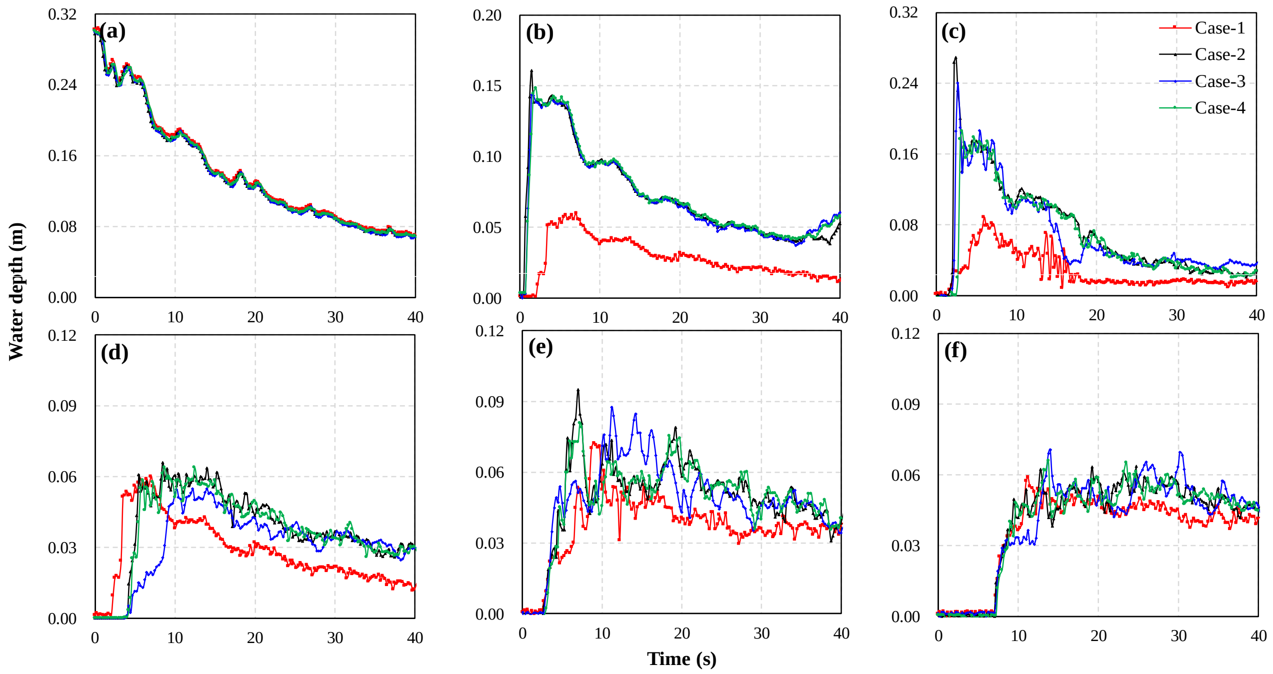

Fig. 8 Comparisons of water depth hydrographs for various street layouts at sites of: (a) P1; (b) P2; (c) P3; (d) P4; (e) P5; (f) P7.

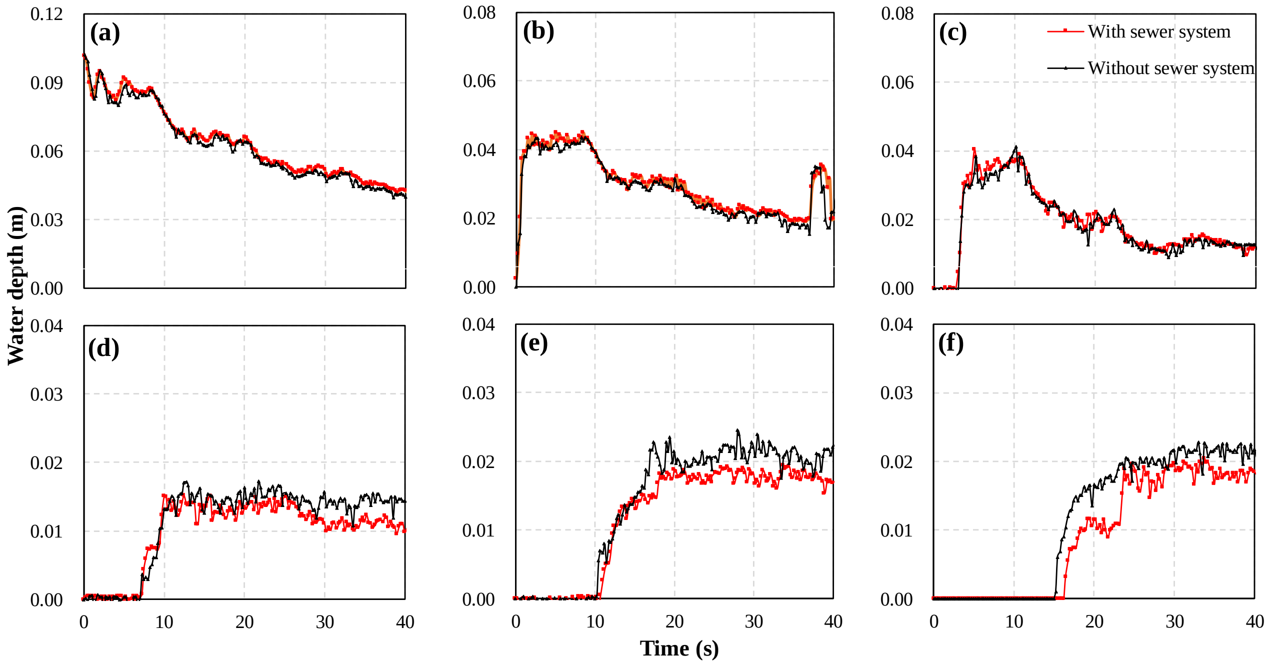

Fig. 9 Effects of the sewer system on water depth variations for the initial water depth of 10 cm (Cases 4 and 6) at sites of: (a) P1; (b) P2; (c) P3; (d) P4; (e) P5; (f) P7.

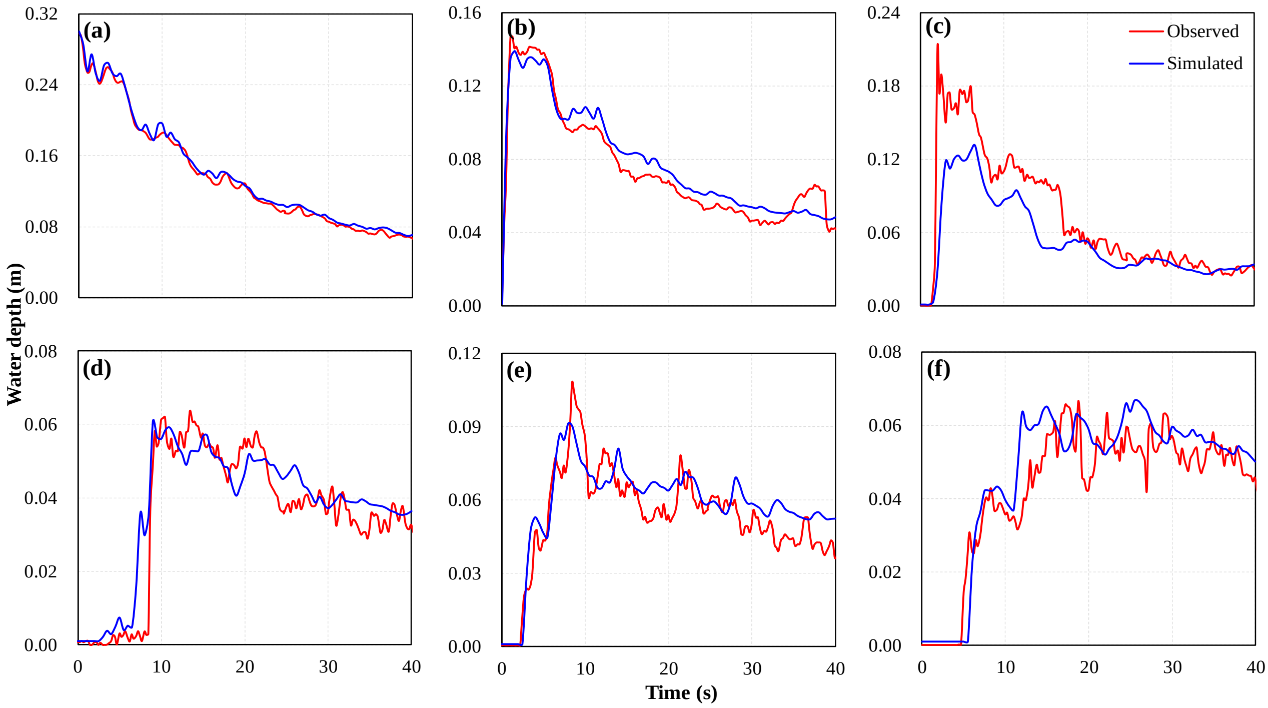

Fig. 10 Comparisons between simulated and observed variations in the water depth hydrographs at sites of: (a) P1; (b) P2; (c) P3; (d) P4; (e) P5; (f) P6.

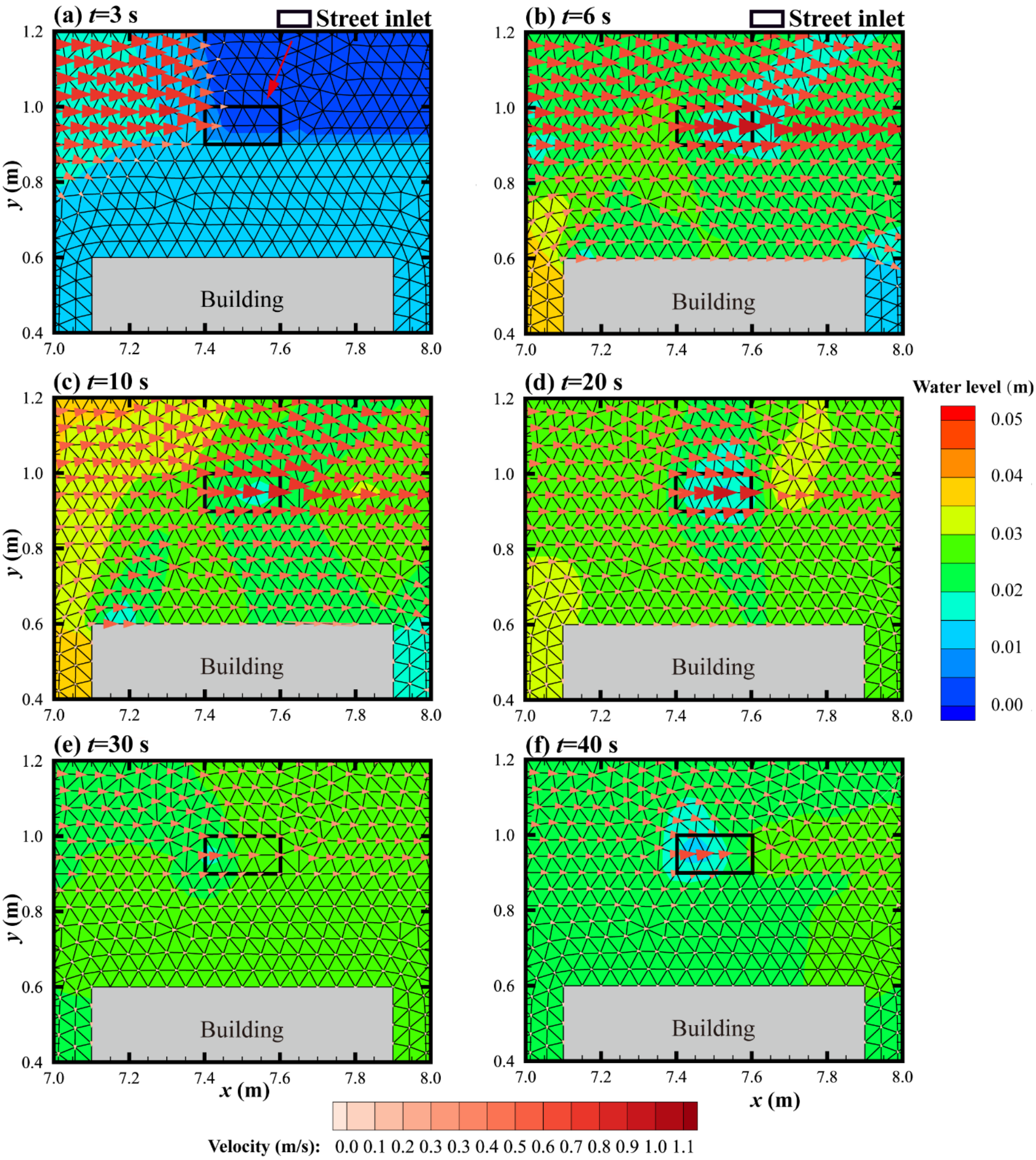

Fig. 11 Velocity fields and water level distributions around the first street inlet for Case 2, for a 30 cm initial water depth at different times of: (a) t=3 s; (b) t=6 s; (c) t=10 s; (d) t=20 s; (e) t=30 s; (f) t=40 s.

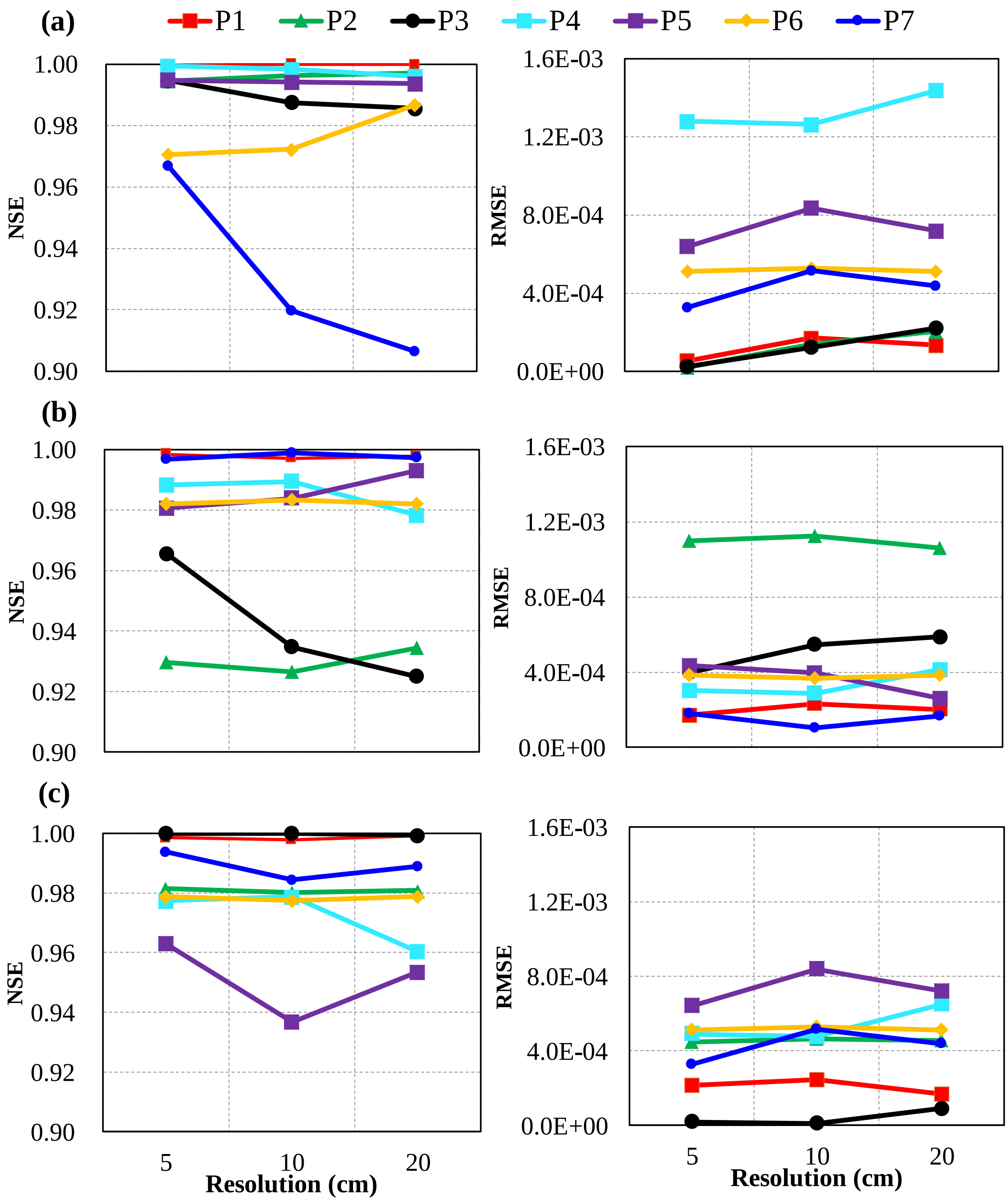

Fig. 12 Model performance variations for different mesh resolutions under initial water depths of: (a) 10 cm; (b) 20 cm; (c) 30 cm.

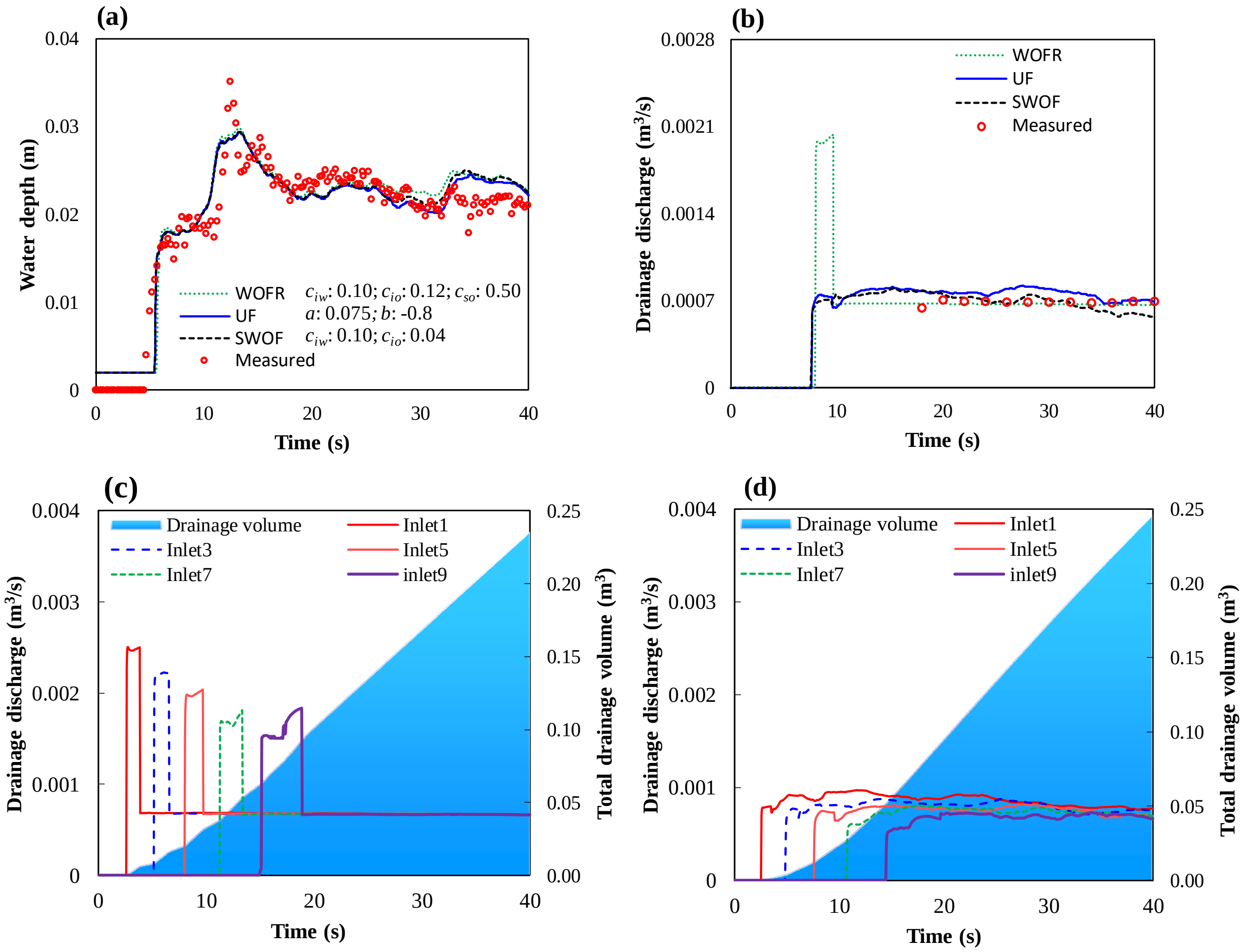

Fig. 13 Simulated hydrographs of surface water depth, drainage discharge and total drainage volume based on different discharge capacity formulae, showing: (a) surface water depth variations at P5; (b) simulated and measured drainage discharges through inlet5; and (c, d) drainage discharge variations along the street direction and total drainage volume obtained using the WOFR and UF, respectively.